Transient Response of Langmuir Turbulence to Abrupt Onset of Surface Heating

Wentao Pan[1] and Qing Li[1,2,*]

[1] *Earth, Ocean and Atmospheric Sciences Thrust, The Hong Kong University of Science and Technology (Guangzhou), Guangzhou, Guangdong, China*

[2] *Guangzhou HKUST Fok Ying Tung Research Institute, Guangzhou, Guangdong, China*

(Dated: January 28, 2026)

Abstract

Langmuir turbulence (LT) plays an important role in enhancing vertical mixing in the ocean surface boundary layer (OSBL). Such enhanced mixing is strongly affected by the diurnally varying heat flux, especially in the early morning when there is a transition from cooling to heating. In this period, turbulence is weakened, yet the surface heat flux is changing rapidly, such that the deviation of transient turbulence from its equilibrium state is large. This may lead to biases in the parameterization of turbulent mixing due to LT in large-scale ocean circulation models, in which an equilibrium of the turbulence state with the surface forcing is often assumed. In this study, we investigate the transient response of LT to an abrupt onset of surface heating using idealized large eddy simulations, and compare it with the transient response of wind-driven shear turbulence (ST). Near the surface, the destabilizing Stokes shear force competes with the stabilizing surface heating, resulting in a gradual decay of the turbulence intensity, in contrast to ST whose intensity decreases rapidly at first and then partially recovers due to the formation of a stronger jet in the surface warm layer. Below the surface, the decay of coherent downwelling plumes of LT occurs faster than shear turbulence, resulting in a quicker response of LT than ST at depth. The vertical velocity variance of LT at depth decays at a rate initially following t^{-1} and later transitioning to t^{-2}. We also examine the impact of details of the Stokes forcing on the transient response of LT. These results may help improve vertical mixing parameterizations in the OSBL.

I. INTRODUCTION

The ocean surface boundary layer (OSBL) serves as a critical interface mediating air-sea exchanges of heat, momentum, and gases through many processes that involve interactions among wind forcing, solar radiation, surface gravity waves, etc. [1, 2]. Among these processes, Langmuir turbulence arising from wave-current interaction via the Craik-Leibovich instability [3–5] is of particular interest due to its significant effects on enhancing vertical mixing in the OSBL and modulating air-sea fluxes [2, 6–9]. However, such a small-scale process in the OSBL is not resolved in large-scale ocean general circulation models (GCM) and its effects require parameterizations. During the past two decades, significant efforts have

* Contact author: ocqingli@hkust-gz.edu.cn

been made to parameterize the effects of Langmuir turbulence in regional and global ocean simulations [10–14], yet large uncertainties persist (see a recent review and comparison in Ref. [15]). In particular, correctly representing OSBL mixing due to Langmuir turbulence during a diurnal cycle remains challenging [16–18].

Under strong diurnal surface heating, a diurnal warm layer (DWL) is formed, trapping heat near the OSBL surface and blocking turbulent exchange with the layer below, so that a diurnal jet develops and shear turbulence is enhanced [19–23]. The presence of Langmuir turbulence inhibits the formation of a DWL due to enhanced turbulent mixing and deepens the DWL when it forms [18, 24]. Existing scalings of the DWL depth work reasonably well in describing the quasi-steady DWL depth around the heating peak during the day [16, 18], but less so when surface heating is changing rapidly, especially in the early morning. Improvement of such scalings requires a better understanding of the transient response of Langmuir turbulence to diurnally varying surface heating.

A typical diurnal cycle in the OSBL consists of distinct phases that can be roughly categorized into the following four [17]. (I) *Nighttime convection*, when the surface condition is largely unstable and convective turbulence develops. (II) *Morning detrainment*, when the surface buoyancy flux transits from unstable to stable as solar radiation begins to increase. As a result, convective turbulence ceases and the resulting entrainment buoyancy flux is suppressed. While the surface becomes stable, the remaining turbulence below the surface decays due to the loss of the driving forces [25], during which weak turbulent mixing may still persists. (III) *Daytime stable boundary layer*, when the daytime solar radiation is strong enough to significantly suppress turbulence driven by surface wind and waves. A balance between the stabilizing effect of solar radiation and the destabilizing effect of wind and waves results in a shallow weakly stratified warm layer [16, 19]. (IV) *Afternoon entrainment*, when solar radiation weakens and its stabilizing effect on turbulence is reduced. Turbulence transits from a stable regime to an unstable regime, driven by a combination of wind, waves, and destabilizing surface buoyancy flux. Strong entrainment occurs at the bottom of the boundary layer, and the boundary layer deepens rapidly.

Existing Langmuir turbulence parameterizations are mostly based on scaling laws derived from a large set of large-eddy simulations (LES) of Langmuir turbulence under steady surface forcing in neutral [26], stable [16], or unstable [13] conditions in a quasi-equilibrium state. These scaling laws describe the equilibrated response of Langmuir turbulence to steady surface forcing. Under time variable forcing, these scaling laws are also expected to be applicable in situations where the surface forcing evolves relatively slowly as compared to the turbulence adjustment time scale, such that turbulence quickly reaches a quasi-equilibrium with the surface forcing. In the context of a diurnal cycle with relatively steady wind and wave forcings, this could happen at both the nighttime in phase (I) and daytime in phase (III), when the surface buoyancy flux varies relatively slowly. This may also apply to afternoon entrainment in phase (IV). Although the surface buoyancy flux transits from stable to unstable rapidly during phase (IV), intense convective turbulence develops because of the destabilizing surface buoyancy flux, which has a relatively short adjustment time scale. In other words, turbulence adjusts sufficiently quickly to the changing forcing, and thus a quasi-equilibrium state may be reached. Indeed, Langmuir turbulence parameterizations based on these scaling laws of quasi-equilibrium responses have fairly good skills in describing turbulent mixing under realistic transient surface forcings, especially in destabilizing surface conditions [15]. However, during morning detrainment in phase (II), surface buoyancy flux transits rapidly from unstable to stable conditions, yet the turbulence intensity is relatively weak and the turbulence adjustment time scale is relatively long. The turbulence may not be able to adjust sufficiently quickly to the rapidly changing surface forcing. Therefore, scaling laws derived from LESs under steady forcing that describe the quasi-equilibrium response may fail [16, 18].

In this study, we focus on the morning detrainment in phase (II). During this phase, the stabilizing solar radiation is rapidly changing, and the boundary layer turbulence is adjusting as a result but cannot reach equilibrium with the forcing. An accurate description of the turbulence state in this scenario requires a good understanding of the transient non-equilibrium response of Langmuir turbulence to continuously changing forcing, which is still lacking. To simplify the problem, here we study the response of Langmuir turbulence to an abrupt onset of surface heating. In addition, we assume that the heating is applied to the surface, in contrast to penetrative solar radiation in reality, which is absorbed in the upper few meters depending on the water turbidity [e.g., 27]. This is an idealized representation of the morning detrainment phase of a diurnal cycle, representing a first step towards a more comprehensive understanding of the transient non-equilibrium response of Langmuir turbulence to rapidly changing surface forcing. In particular, we conduct idealized LES experiments to study the transient evolution of the intensity and structure of Langmuir turbulence after an abrupt onset of surface heating. We also contrast the transient response of Langmuir turbulence with that of wind-driven shear turbulence to better understand the effect of surface waves.

The remainder of this paper is structured as follows. Section II describes the configuration of the LES model and the setup of the experiments. The time evolution of the intensity and structure of Langmuir turbulence after the abrupt onset of surface heating are discussed and compared with those of wind-driven shear turbulence in Section III. The impact of details in the surface wave forcing is also explored. This paper ends with a brief discussion and the main conclusions in Section IV.

II. METHODS

A. Model Description

The idealized LES experiments in this study are performed using Oceananigans (v0.91.5), a Julia-based GPU-accelerated software package for numerical simulations of geophysical fluid dynamics [28, 29]. Oceananigans utilizes a finite-volume spatial discretization scheme and offers flexible configurations for LES through various combinations of subgrid-scale (SGS) closures, advection schemes, and time-stepping methods. While relatively new, it has gradually gained popularity in ocean modeling and has been used in solving various problems in geophysical fluid dynamics, including modeling ocean surface boundary layer turbulence under different forcing conditions [29–34].

Using the `NonhydrostaticModel` in Oceananigans, we solve the wave-averaged Boussinesq equation, or the Craik-Leibovich (CL) equation [3, 4], written as a prognostic equation for the Lagrangian velocity [35, 36],

$$\partial_t \mathbf{u}^L + (\mathbf{u}^L \cdot \nabla)\mathbf{u}^L = -(f\hat{\mathbf{z}} - \nabla \times \mathbf{u}^S) \times \mathbf{u}^L - \nabla p + b\hat{\mathbf{z}} + \mathcal{D}^{\mathbf{u}} + \partial_t \mathbf{u}^S, \tag{1}$$

$$\nabla \cdot \mathbf{u}^L = 0, \tag{2}$$

$$\partial_t b + (\mathbf{u}^L \cdot \nabla) b = \mathcal{D}^b, \tag{3}$$

where f is the Coriolis parameter, $\hat{\mathbf{z}}$ is the vertical unit vector, p is the kinematic pressure, b is the buoyancy, and $\mathcal{D}^{\mathbf{u}}$ and $\mathcal{D}^b$ are the SGS diffusion of momentum and buoyancy. The Lagrangian velocity $\mathbf{u}^L = \mathbf{u} + \mathbf{u}^S$ is the sum of the Eulerian velocity $\mathbf{u}$ and Stokes drift

$\mathbf{u}^S$. Stokes drift for a monochromatic deep-water wave aligned with the wind direction (x-direction) can be written as

$$\mathbf{u}^S(z) = \omega k A^2 e^{2kz}\hat{\mathbf{x}}, \tag{4}$$

where ω is the angular frequency, $k = \omega^2/g$ is the wavenumber, g is the gravitational acceleration, A is the wave amplitude, and $\hat{\mathbf{x}}$ is a unit vector in x-direction. It is assumed that $\mathbf{u}^S$ is not affected by turbulent motions (thus prescribed following (4)) and remains constant in time ($\partial_t \mathbf{u}^S = 0$). In this study, equations (1)-(3) are solved in Oceananigans using a combination of the anisotropic minimum dissipation closure scheme [37], the fifth-order WENO advection scheme, and the third-order Runge-Kutta time-stepping method with adaptive time step according to the Courant-Friedrichs-Lewy condition. Sensitivity tests using the ninth-order WENO advection scheme without an explicit SGS closure [e.g., 38] show similar results, especially in the presence of Langmuir turbulence (not shown), which increases the turbulent length scale and reduces the sensitivity of the resolved turbulent flow to the SGS closure under stabilizing surface heating.

B. Experimental Design

Idealized LES experiments are guided by classical LES studies of Langmuir turbulence [e.g., 6]. The surface wind forcing is given by a constant surface wind stress τ in the x-direction with a friction velocity $u_* = \sqrt{\tau/\rho_o} = 6.1 \times 10^{-3}$ m s^{-1}, corresponding to a surface wind speed of 5 m s^{-1}. Without surface wave forcing, this generates classical wind-driven shear turbulence (hereafter denoted by ST). Typical Langmuir turbulence as in Ref. [6] is generated with the same wind forcing, but is additionally driven by a steady Stokes drift profile aligned with the surface wind according to (4) with wavenumber $k = 2\pi/60$ m^{-1} and wave amplitude $A = 0.8$ m (hereafter denoted by LT). This yields a surface Stokes drift $u_0^S \approx 6.8 \times 10^{-2}$ m s^{-1}, corresponding to a turbulent Langmuir number $\mathrm{La}_t = (u_*/u_0^S)^{1/2} \approx 0.3$, and an e-folding decay depth of the Stokes drift profile $\delta^S = 1/2k \approx 4.8$ m. Additional experiments are carried out with different La_t but the same δ^S (LT2 and LT3), and different δ^S but the same La_t (LT4 and LT5). The forcing parameters of all experiments are summarized in Table I.

Under these horizontally homogeneous forcing conditions, wind-driven shear turbulence or Langmuir turbulence quickly develops in the initial mixed layer of 33 m and erodes into

TABLE I. A summary of forcing parameters in the idealized LES experiments. Shown are the wavenumber k, wave amplitude A, turbulent Langmuir number La_t, e-folding decay depth of Stokes drift δ^S, initial mixed layer at the onset of surface heating h_i (defined by the depth where $\overline{w'b'}$ reaches its minimum), and surface heat fluxes.

	k (m^{-1})	A (m)	La_t	δ^S (m)	h_i (m)	Q_0 (W m^{-2})
ST	-	-	-	-	30.0	50, 100, 200, 400, 800
LT	$2\pi/60$	0.8	0.3	4.8	31.5	50, 100, 200, 400, 800
LT2	$2\pi/60$	0.533	0.45	4.8	31.0	50, 200, 800
LT3	$2\pi/60$	0.4	0.6	4.8	30.8	50, 200, 800
LT4	$2\pi/30$	0.476	0.3	2.4	30.8	50, 200, 800
LT5	$2\pi/15$	0.283	0.3	1.2	31.0	50, 200, 800

a constant stratification $\partial_z \overline{b} = N_0^2 = 10^{-4}$ s^{-2} below. Here we use an overline $\overline{()}$ to denote the horizontal average, and later a prime $()'$ to denote the deviation from the horizontal average. No surface buoyancy flux is imposed during the first 64 hours of these simulations, allowing wind-driven shear turbulence or Langmuir turbulence to develop fully before the abrupt onset of surface heating (defined as $t = 0$) with various strengths (Table I). A linear equation of state with a thermal expansion coefficient $\alpha = 2 \times 10^{-4}$ °C^{-1} is assumed to link the surface heat flux Q_0 (defined as positive for surface warming) and the surface buoyancy flux $B_0 = -\alpha g Q_0 / c_p \rho_o$, where $c_p = 3991$ J kg^{-1} °C^{-1} and $\rho_o = 1026$ kg m^{-3} are the specific heat and density of seawater. All experiments continue for another 48 hours after the abrupt onset of surface heating, and horizontally averaged fields and turbulent statistics are recorded at 3-minute intervals for subsequent analysis.

The Coriolis parameter is defined as $f = 2\pi/T_f$ with an inertial period $T_f = 57600$ s (16 hours), corresponding to a latitude of 48.6°N. To minimize the unwanted inertial oscillation associated with a sudden onset of the surface wind, which is unbalanced with the initial zero Lagrangian velocity, the surface wind stress is smoothly initialized in all simulations using a time-dependent scaling factor following Ref. [39],

$$F(t) = \begin{cases} \frac{1}{2}\left[1 - \cos\frac{\pi t}{T_0}\right], & 0 \le t \le T_0, \\ 1, & t > T_0, \end{cases} \tag{5}$$

where $T_0 = 86400$ s. This smooth onset of surface wind forcing effectively eliminates inertial oscillation in the simulated horizontal velocity fields (see Appendix A). Note that inertial oscillation is inevitably generated when an abrupt onset of surface heating is imposed. However, this smooth onset of surface wind forcing during the spinup phase ensures that no inertial oscillation preexists that may complicate the diagnosed response of Langmuir turbulence to the abrupt onset of surface heating.

All simulations are conducted in a computational domain of 256 m $\times$ 256 m $\times$ 64 m, evenly discretized into 512 $\times$ 512 $\times$ 256 grid boxes. The corresponding horizontal grid spacing is $\Delta x = \Delta y = 0.5$ m and the vertical grid spacing is $\Delta z = 0.25$ m. Testing confirmed that this resolution is sufficient to resolve the energy-carrying eddies and resulting turbulent fluxes due to wind-driven shear turbulence and Langmuir turbulence. While a much higher resolution may be required to accurately describe small scale turbulence under strong surface heating conditions in a quasi-equilibrium state, the resolution used here is sufficient to describe the transient stage. The computational domain is doubly periodic in the horizontal directions. A sponge layer nudging the velocity and buoyancy to their initial values is used near the bottom to avoid the reflection of internal waves [29].

III. RESULTS

We focus our discussion of the transient response of Langmuir turbulence to abrupt onset of surface heating in the LT case, contrasting the results with wind-driven shear turbulence in the ST case wherever appropriate. We also examine the impact of details of the Stokes forcing with the help of other LT cases.

A. An Overview of the Transient Response

As an example, Fig. 1 compares the time evolution of horizontally averaged and normalized stratification, squared vertical shear of horizontal Lagrangian velocity, vertical velocity variance, and vertical buoyancy flux in the LT and ST cases before and after the abrupt onset of surface heating with $Q_0 = 200$ W m^{-2}. The near-surface stratification quickly increases in response to the onset of surface heating in the ST case (Fig. 1e), blocking the connection between the surface where wind forcing is applied and the layers below. This results in a sudden drop in turbulence intensity near the surface (as indicated by the vertical velocity variance $\overline{w'^2}$ in Fig. 1g). However, the intensity of near-surface turbulence partially recovers quickly due to the development of strong velocity shear (Fig. 1f) as the momentum input from the wind is now trapped in a much shallower surface warm layer, as well as the buoyancy input from the surface heating which enhances the near-surface stratification (Fig. 1h). This mechanism is well-understood, which explains the formation of the DWL and a diurnal jet [21–23]. In contrast, in the LT case, the presence of Langmuir turbulence inhibits the formation of strong stratification near the surface (Fig. 1a) that suppresses turbulence. Therefore, the turbulence intensity does not exhibit a sudden drop as severely as in the ST case (Fig. 1c) and the resulting warm layer is much deeper than in the ST case, in which the momentum is more well mixed (Fig. 1b) and the surface heat flux is distributed to a deeper depth (Fig. 1d).

Significantly different responses are also seen below the surface between the LT and ST cases. With abrupt onset of surface heating, while the turbulence below the surface is blocked from the surface wind forcing in the ST case and decays slowly with a time scale that increases with depth (Fig. 1g), the decay of the turbulence below the surface in the LT case occurs more rapidly and does not exhibit a strong dependence on depth (Fig. 1c). This is probably due to the fact that, in the LT case, the surface and the layer below are more well connected than in the ST case by coherent Langmuir turbulence that extends deeply in the mixed layer. An abrupt surface heating weakens the driving force for these coherent turbulence structures, leading to an immediate response to the changes of surface forcing throughout the mixed layer. As a result, the decaying coherent Langmuir turbulence in the LT case also contributes to a burst of vertical buoyancy flux that exceeds its equilibrium value right after the abrupt onset of surface heating (Fig. 1d, around $t = 1$ h), which is not seen in the ST case (Fig. 1h).

Within a few hours after the abrupt onset of surface heating, the destabilizing Langmuir turbulence and stabilizing surface heating in the LT case reach a quasi-equilibrium, and the mixed layer depth slowly transitions to its equilibrium value (black cross sign in Fig. 1d). Note that the mixed layer depth in the heating phase is defined as the depth where $\overline{w'b'} = 0.05B_0$, in contrast to the initial phase before surface heating, where it is defined as the depth where $\overline{w'b'}$ reaches its minimum (horizontal dotted lines in Fig. 1). This definition is roughly consistent with the definition in Ref. [16], in which a linear fit of the $\overline{w'b'}$ profile was

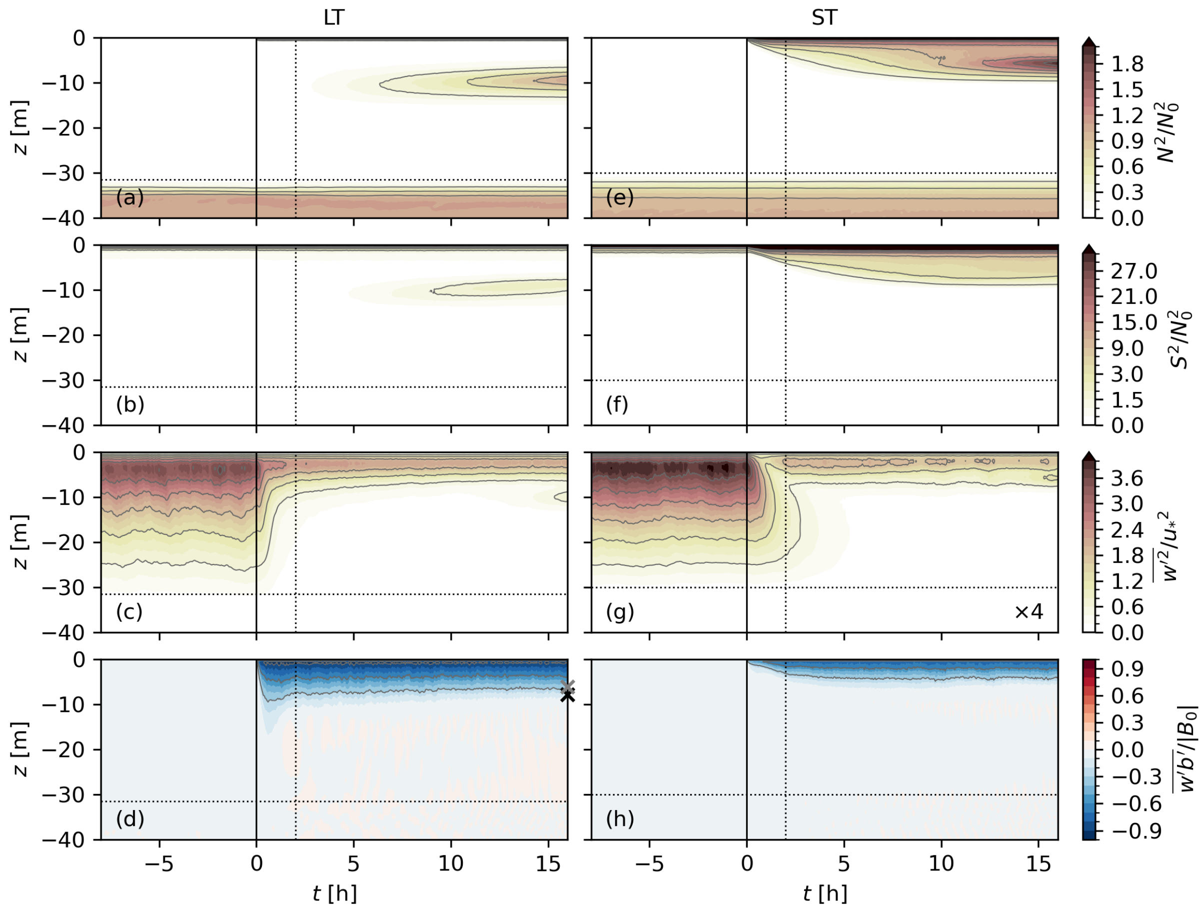

FIG. 1. Time evolution of the horizontally averaged (a,e) stratification $N^2 = \partial_z \bar{b}$ normalized by the stratification below the mixed layer N_0^2, (b,f) squared vertical shear of horizontal Lagrangian velocity $S^2 = \left[(\partial_z \overline{u}^L)^2 + (\partial_z \overline{v}^L)^2\right]$ normalized by N_0^2, (c,g) vertical velocity variance $\overline{w'^2}$ normalized by the surface friction velocity u_*, and (d,h) buoyancy flux $\overline{w'b'}$ normalized by the magnitude of the surface buoyancy flux $|B_0|$ in the (a-d) LT and (e-h) ST cases, before and after the abrupt onset of surface heating with $Q_0 = 200$ W m^{-2}. Horizontal dotted lines mark the initial mixed layer depth $z = -h_i$ at the onset of surface heating and vertical dotted lines denote the time ($t = 2$ h) when snapshots of w in Figs. 2 and 3 are taken. Black and gray cross signs in panel (d) mark the equilibrium mixed layer depth diagnosed in the simulation (see the text for the definition) and according to the scaling of Ref. [16], respectively. To enhance clarity, selected contours are shown (corresponding to the labeled values excluding 0.0 in the respective colorbar), a two-part color scale (two linear scales below and above 3.0) is used for S^2, and $\overline{w'^2}$ in the ST case in panel (g) is multiplied by a factor of 4.

used and the mixed layer depth was defined as the depth at which the fitted line reaches zero. For reference, the equilibrium mixed layer depth according to the scaling in Ref. [16] is also marked (gray cross sign in Fig. 1d). The equilibrium mixed layer depth in our simulations, taken as the average over the last inertial period (from $t = 32$ h to $t = 48$ h), and the scaling in Ref. [16] are compared for all cases in Appendix B.

B. Suppression of Vertical Motions by Surface Heating

Fig. 2 shows snapshots of the simulated vertical velocity in the LT case at different depths at $t = 0$ h and $t = 2$ h, illustrating the effects of the abrupt onset of surface heating with different strengths on the intensity and structure of Langmuir turbulence. Characteristic structures of Langmuir turbulence [6] are clearly seen before the onset of surface heating, with stripes of downwelling regions roughly aligning with the wind and waves and slightly veering to the right due to the Coriolis force near the surface (Fig. 2a). These elongated downwelling regions merge and grow in size at deeper depths (Fig. 2e), veering further to the right and leaving a strong signature even near the base of the mixed layer (Fig. 2i). The deeply penetrating plumes of Langmuir turbulence [40] are reminiscent of convective plumes and have a similar impact on the anisotropy of turbulence [39]. Indeed, these plume-like structures contribute significantly to the vertical transport of turbulent kinetic energy (TKE) in the mixed layer [6], and distinguish Langmuir turbulence from wind-driven shear turbulence [39]. As shown in Fig. 3, which shows the snapshots of the simulated vertical velocity in the ST case, wind-driven shear turbulence exhibits smaller and more isotropic turbulence structures than Langmuir turbulence, especially below the surface.

Two hours of relatively weak surface heating with $Q_0 = 50$ W m^{-2} does not change the near-surface turbulence structure too much in the LT case (Fig. 2b). Even with $Q_0 = 200$ W m^{-2}, the small scale stripes of downwelling regions are not very different from that before the heating (Fig. 2c). Only when the surface heating is sufficiently strong with $Q_0 = 800$ W m^{-2}, these characteristic turbulence structures collapse (Fig. 2d). This is consistent with Ref. [41] which reported that the breakdown of Langmuir cells under surface heating occurs when the Hoenikker number $\mathrm{Ho} = 2B_0/(ku_0^S u_*^2)$ reaches $\sim 1{-}2$. Here, $\mathrm{Ho} = [0.18, 0.72, 2.90]$ for the LT case with surface heating of $Q_0 = [50, 200, 800]$ W m^{-2}.

Near the surface, the vertical shear of the Stokes drift is strong. So, there is direct

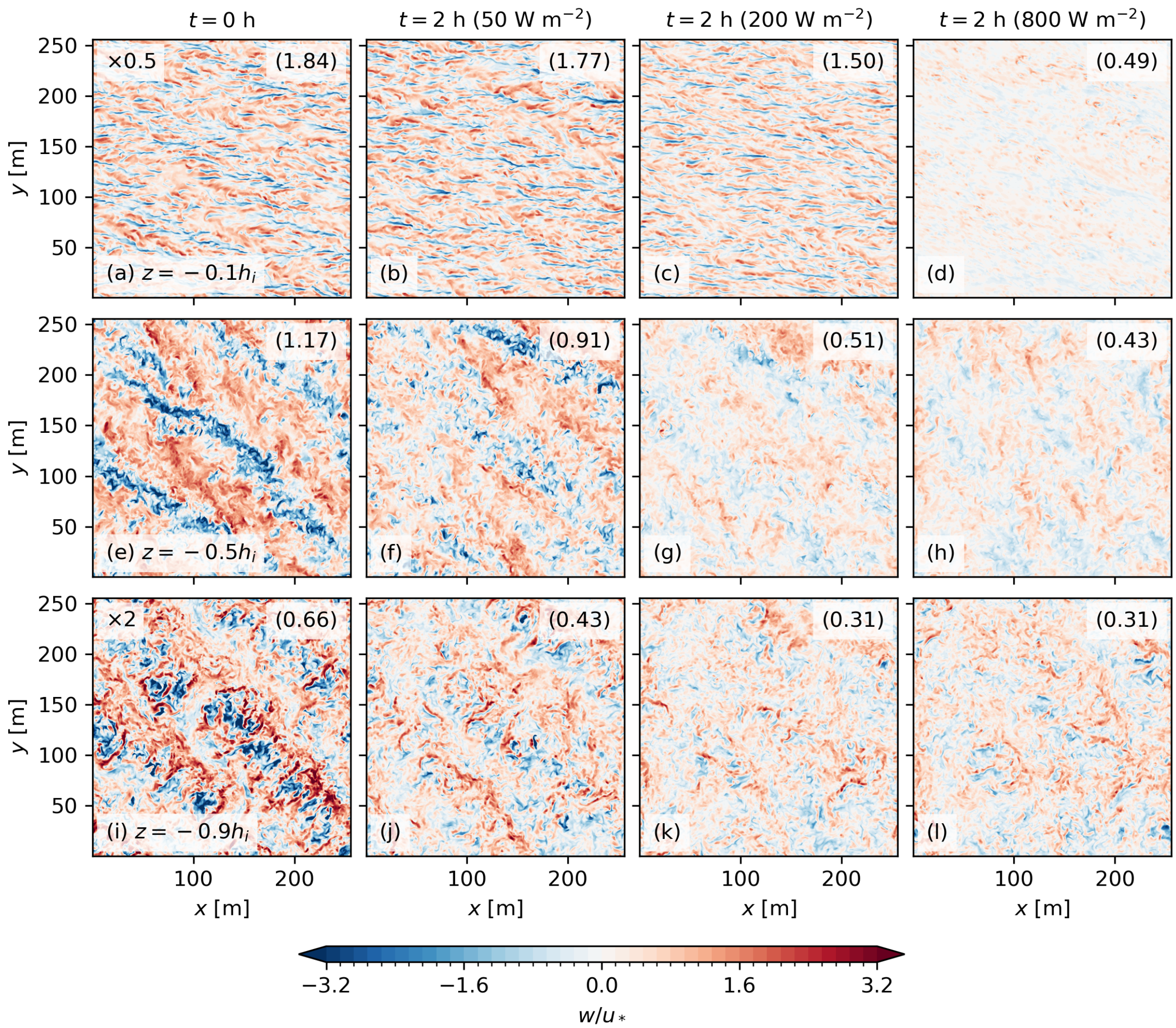

FIG. 2. Snapshots of normalized vertical velocity w/u_* illustrating the impact of abrupt onset of surface heating on the turbulence intensity and structure in the LT case. Different rows show snapshots at different depths: (a–d) $z = -0.1h_i$, (e–h) $z = -0.5h_i$, and (i–l) $z = -0.9h_i$. The left column (a,e,i) shows the snapshots before the onset of surface heating ($t = 0$ h), and the other three columns show the snapshots after 2 hours of surface heating for the cases of (b,f,j) $Q_0 = 50$ W m^{-2}, (c,g,k) $Q_0 = 200$ W m^{-2}, and (d,h,l) $Q_0 = 800$ W m^{-2}. Numbers in parentheses in each panel show the root-mean-square value of the normalized vertical velocity. To highlight the turbulence structure, the vertical velocity in (a–d) and (i–l) are multiplied by 0.5 and 2, respectively, when plotting using the same color scale as (e–h).

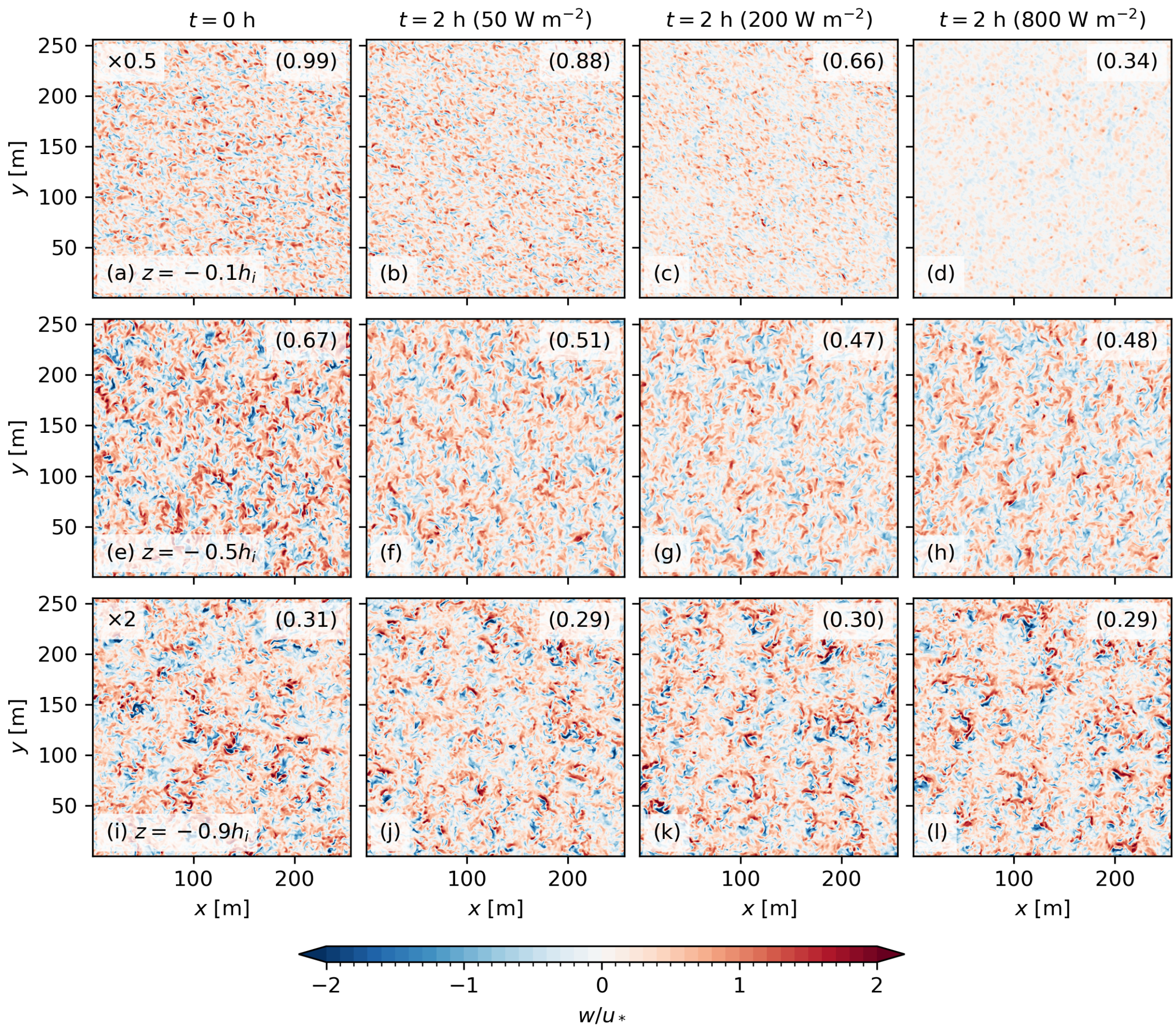

FIG. 3. Same as Fig. 2, but for the ST case.

competition between the destabilizing CL vortex force [3, 4] (more intuitively, the Stokes shear force [36]) and the stabilizing surface heating [41]. The CL instability makes the near-surface turbulence structures more resilient than wind-driven shear turbulence to the stabilizing effect of surface heating. For example, two hours of surface heating with $Q_0 = 200$ W m^{-2} reduces the root-mean-square (RMS) vertical velocity at $z = -0.1h_i$ by $\sim 18\%$ in the LT case (Fig. 2c), compared to over 33% in the ST case (Fig. 3c).

Below the surface, the turbulence intensity in the LT case is more prone to the effects of surface heating. The RMS vertical velocity is reduced by 56% at $z = -0.5h_i$ and 53% at $z = -0.9h_i$ after two hours of surface heating with $Q_0 = 200$ W m^{-2} (Fig. 2g,k). Further increasing the surface heating strength to $Q_0 = 800$ W m^{-2} does not change the results too much (Fig. 2h,l). This is due to the fact that the driving force of the downwelling plumes in Langmuir turbulence is the downward push by the Stokes shear force, which is mainly confined near the surface where Stokes drift shear is strong [36]. Without stable stratification, these downwelling plumes can penetrate deeply throughout the mixed layer [40]. With sufficiently strong surface heating, the resulting stable stratification inhibits the formation and penetration of these downwelling plumes, just as in the case of convective turbulence. Turbulence away from the surface is effectively blocked from its driving force and freely decays, while largely preserving its structure (e.g., elongated downwelling regions similar to those before surface heating are still visible in Fig. 2g). In contrast, wind-driven shear turbulence at depth is not as tightly connected to the surface forcing as Langmuir turbulence. It also has a much smaller spatial scale than Langmuir turbulence. Therefore, the decay of wind-driven shear turbulence below the surface is much slower (Fig. 3e-l).

These different responses to the abrupt onset of surface heating between Langmuir turbulence and wind-driven shear turbulence can also be seen from the pre-multiplied energy spectrum kE_w of the vertical velocity w in Fig. 4. Note that the energy spectrum E_w is multiplied by the wavenumber k here, so the area below the curve kE_w reflects the energy contributed by the wavenumber k on the logarithmic scale. After two hours of relatively weak surface heating with $Q_0 = 50$ W m^{-2} (dashed lines in blue), changes in the pre-multiplied energy spectrum are small in the ST case, with stronger reductions at $z = -0.5h_i$ (Fig. 4e) than at $z = -0.5h_i$ and $z = -0.9h_i$. In the LT case, however, reductions in vertical velocity variance on relatively large scales are clearly seen at $z = -0.5h_i$ (Fig. 4b) and more pronounced over all scales at $z = -0.9h_i$ (Fig. 4c). With stronger surface heating $Q_0 = 200$ W m^{-2} (dashed lines in orange), the further reductions in vertical velocity variance on the energy-containing scales are greater near the surface and barely seen at deeper depths in the ST case. In contrast, the further reductions are greater at $z = -0.5h_i$ and $z = -0.9h_i$ than at $z = -0.1h_i$ in the LT case. In addition, these reductions occur at all scales at deeper depths, in contrast to only large scales near the surface. The energy-containing scales near the surface in the LT case correspond to the stripes of roll structures that characterize Langmuir turbulence, which persist after two hours of surface heating with $Q_0 = 200$ W m^{-2} (Fig. 2c). The collapse of Langmuir turbulence under strong surface heating with $Q_0 = 800$ W m^{-2} (Fig. 2d) is reflected in the pre-multipiled energy spectrum as a reduction of vertical velocity variance over all scales near the surface, especially over the

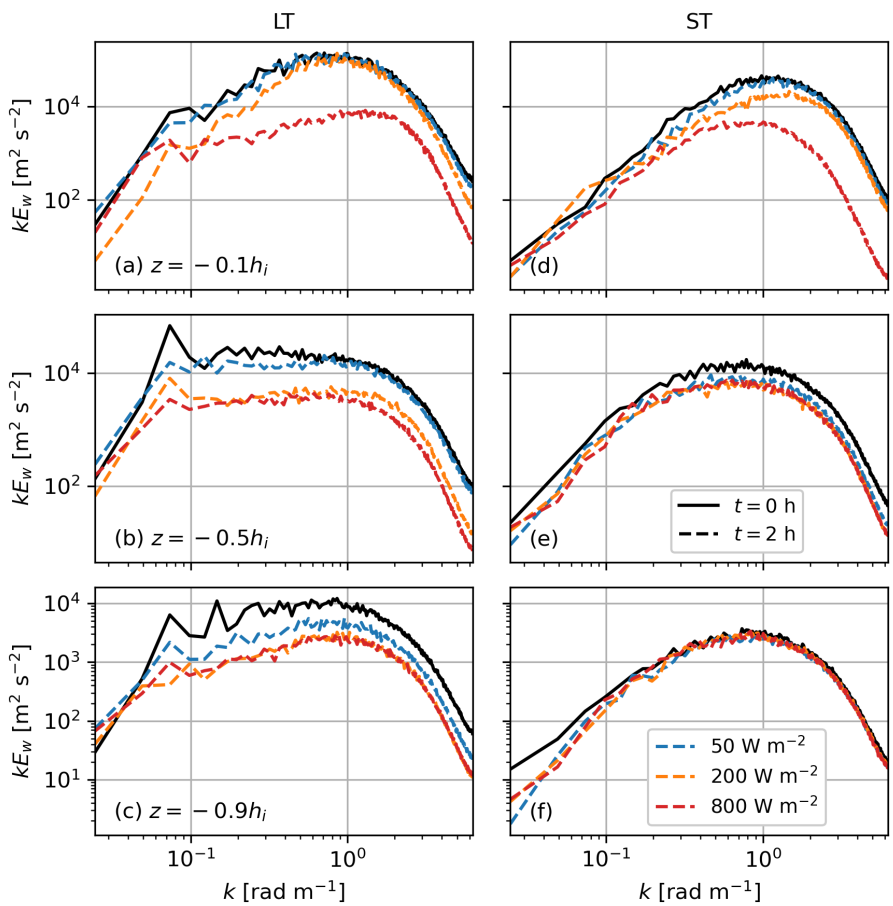

FIG. 4. Pre-multiplied energy spectrum of the vertical velocity w at (a,d) $z = -0.1h_i$, (b,e) $z = -0.5h_i$, and (c,f) $z = -0.9h_i$ for the (a–c) LT and (d–f) ST cases, corresponding to the vertical velocity snapshots in Figs. 2 and 3. Solid and dashed lines show the spectrum before ($t = 0$ h) and after ($t = 2$ h) the onset of surface heating, respectively. Different heating scenarios with $Q_0 = 50$ W m^{-2}, $Q_0 = 200$ W m^{-2}, and $Q_0 = 800$ W m^{-2} are shown in blue, orange, and red, respectively.

energy-containing scales (dashed line in red in Fig. 4a). At deeper depths, a stronger surface heating does not make much difference beyond $Q_0 = 200$ W m^{-2}, suggesting a complete blocking of the driving force for the characteristic deeply penetrating plumes of Langmuir turbulence with intermediate surface heating. In the ST case, the small-scale vertical velocity variance near the surface continues to drop in response to the strong surface heating (dashed line in red in Fig. 4d), and no significant changes are observed at deeper depths.

C. Transient Response of TKE and Turbulence Anisotropy

Fig. 5 shows the transient response of TKE, defined as $e = \frac{1}{2}\left(\overline{u'^2} + \overline{v'^2} + \overline{w'^2}\right)$, and its three components to the abrupt onset of surface heating with $Q_0 = 200$ W m^{-2} at different depths. Near the surface at $z = -0.1h_i$, the TKE in the LT case decays exponentially with time after the onset of surface heating (Fig. 5a). The dominance of $\overline{w'^2}$ and $\overline{v'^2}$ over $\overline{u'^2}$, which distinguishes Langmuir turbulence from wind-driven shear turbulence with $\overline{u'^2} > \overline{v'^2} > \overline{w'^2}$ as shown in Fig. 5d, persists, consistent with the persistence of small-scale stripes of the downwelling regions in Fig. 2c. In the ST case, there is an initial decay of the TKE to less than 1/2 of its initial value at a rate faster than that of the LT case until around $t = 1$ h, after which the TKE recovers quickly to around 3/4 of its initial value within an hour and stays stable afterward. The relative importance of its three components also remains roughly unchanged, consistent with the turbulence structures in Fig. 3c.

Below the surface at both $z = -0.5h_i$ and $z = -0.9h_i$, the TKE remains unchanged for a while before decaying exponentially over time. Consistent with Fig. 1c,g, the TKE remains unchanged longer in the ST case than in the LT case (Fig. 3e,f versus Fig. 3b,c), and at deeper depth than at shallower depth (Fig. 3c,f versus Fig. 3b,e). While the relative importance of the three components of the TKE remains roughly unchanged in the ST case (except the relative importance of $\overline{u'^2}$ and $\overline{v'^2}$, which may be related to the development of an inertial oscillation of the velocity shear), $\overline{w'^2}$ decays faster than the other two components in the LT case. At $z = -0.5h_i$, $\overline{w'^2}$ quickly stops dominating the TKE about half an hour after the onset of surface heating (Fig. 5b). At $z = -0.9h_i$, $\overline{w'^2}$ is the smallest before the onset of surface heating and becomes even smaller afterward (Fig. 5c). These changes in the anisotropy of the turbulence in the LT case below the surface are due to the faster decay of large-scale roll structures of Langmuir turbulence than small-scale turbulence, which are driven nonlocally from the surface where Stokes drift shear is strong, as shown in Fig. 2g.

To better understand the transient response of the TKE to the abrupt onset of surface heating, we also analyze the TKE budget. The budget equation for the TKE is [e.g., 6],

$$\partial_t e = \underbrace{-\overline{w'\mathbf{u}'_h} \cdot \partial_z \overline{\mathbf{u}}_h}_{P} \underbrace{-\overline{w'\mathbf{u}'_h} \cdot \partial_z \mathbf{u}^S}_{P^S} \underbrace{+\overline{w'b'}}_{B} \underbrace{-\partial_z \overline{w'p'} - \partial_z \overline{w'e}}_{T} \underbrace{-\varepsilon}_{D}, \tag{6}$$

where $\mathbf{u}_h = [u, v]$ is the horizontal component of the velocity. The terms on the right-hand side are shear production (P), Stokes production (P^S), buoyancy production (B), pressure

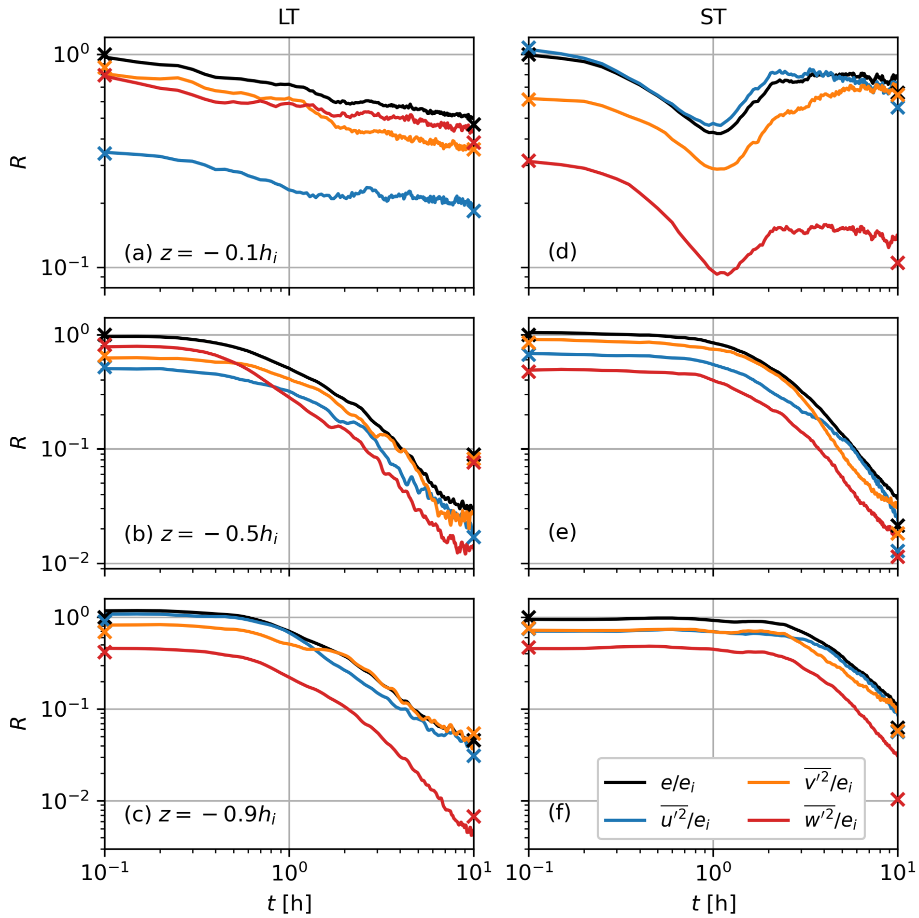

FIG. 5. Transient response of the TKE (black lines) and its three components (colored lines) to the abrupt onset of surface heating with $Q_0 = 200$ W m^{-2} at (a,d) $z = -0.1h_i$, (b,e) $z = -0.5h_i$, and (c,f) $z = -0.9h_i$ in the (a–c) LT and (d–f) ST cases. Cross signs at the left and right sides of each panel mark the mean values averaged over an inertial period before the onset of surface heating (from $t = -16$ h to $t = 0$ h) and at the end of the simulations (from $t = 32$ h to $t = 48$ h), respectively. All quantities are normalized by the initial mean TKE e_i before the heating. Note that both axes are in logarithmic scale.

correlation and TKE transport terms (T), and dissipation (D).

The transient evolution of these TKE budget terms at different depths in the LT and ST cases after an abrupt onset of surface heating with $Q_0 = 200$ W m^{-2} is shown in Fig. 6. Near the surface at $z = -0.1h_i$, Stokes production still dominates the TKE source in the LT case after the onset of heating, and shear production still dominates the TKE source in the ST case. The magnitude follows the trend of the TKE in Fig. 5. This suggests that Langmuir

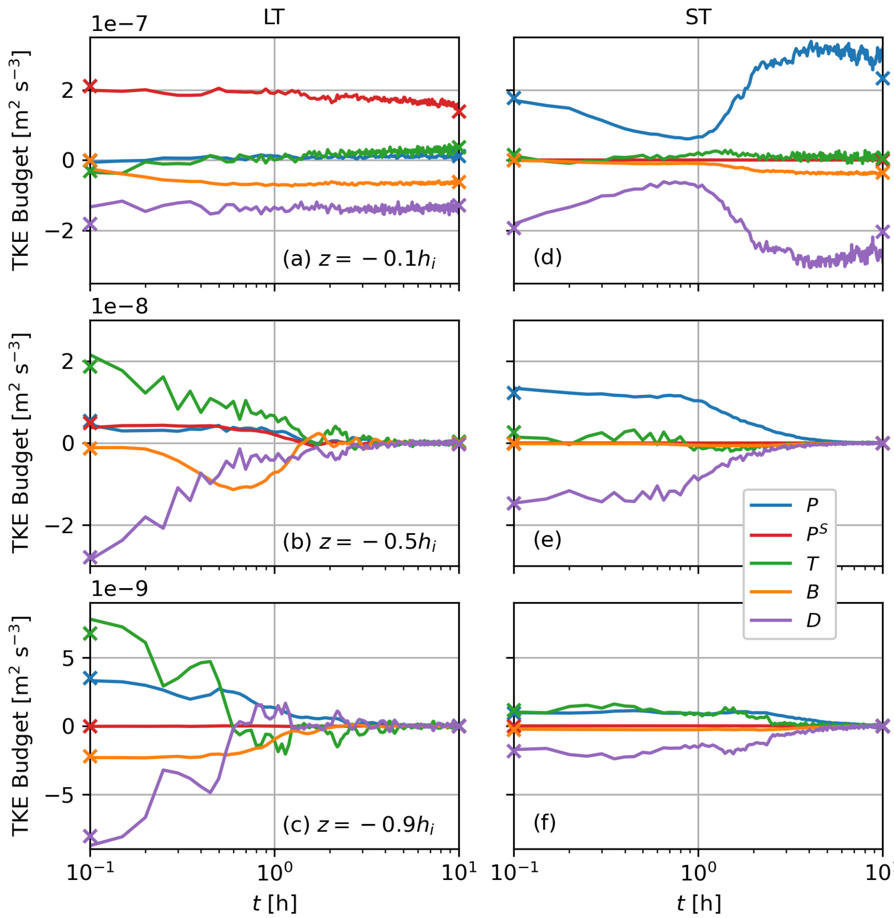

FIG. 6. Same as Fig. 5, but for the TKE budget terms in Eq. (6), shown by lines in different colors. Note that, unlike Fig. 5, the horizontal axis is in logarithmic scale but the vertical axis is in linear scale.

turbulence in the LT case and wind-driven shear turbulence in the ST case are weakened but not completely shut down by surface heating. Note that with $Q_0 = 800$ W m^{-2}, the dominant TKE source in the LT case changes from Stokes production to shear production after about 1 hour of surface heating (not shown), consistent with the breakdown of Langmuir cells in Fig. 2d. Interestingly, the buoyancy production, which serves as a sink of TKE due to the stabilizing surface heating, is playing a much bigger role in the LT case than in the ST case (orange lines in Fig. 6a,d), especially immediately following the onset of surface heating (e.g., before $t = 1$ h). This is due to the coherent rolls of Langmuir turbulence that effectively transport heat downward, inhibiting the formation of a shallow warm layer with strong stratification, which strongly suppresses turbulence in the ST case before strong shear develops but not in the LT case. Another interesting feature in the TKE budget in the LT case is the transition of the TKE transport term from a sink before the surface heating to a source after (green line in Fig. 6a). This may result from a shoaling of the mixed layer, in which case the coherent rolls of Langmuir turbulence are restricted by the stratification and unable to transport TKE generated near the surface down to a deeper depth.

Below the surface at both $z = -0.5h_i$ and $z = -0.9h_i$, TKE transport still dominates the TKE source in the LT case, but its magnitude rapidly decays over time. Shear production plays an increasingly important role at $z = -0.9h_i$ as TKE transport decays faster than shear production (Fig. 6c). In the ST case, shear production dominates the TKE source at $z = -0.5h_i$ and TKE transport dominates at $z = -0.9h_i$. However, unlike the rapid decay of the TKE source in the LT case, shear production remains roughly unchanged for around 1 hour at $z = -0.5h_i$ and almost 3 hours at $z = -0.9h_i$ before decaying at a faster rate. The TKE transport also decays much slower than in the LT case. Note that the distinction of the buoyancy production term between the LT and ST cases is more pronounced than near the surface. In particular, there is a burst of $\overline{w'b'}$ at $z = -0.5h_i$ that peaks around $t = 0.6$ h (Fig. 6b) in the LT case, but not in the ST case. This burst of $\overline{w'b'}$ can be clearly seen in Fig. 1d, which extends over depths roughly from $z = -8$ m to $z = -18$ m. This is the result of the decaying downwelling plumes of Langmuir turbulence (e.g., Fig. 2g) that transport positive buoyancy due to surface heating downward (thus $\overline{w'b'} < 0$).

D. Impact of Surface Wave Forcing

The turbulent structure of Langmuir turbulence depends not only on the surface Stokes drift [42], but also on the decay length scale of Stokes drift [43]. To examine to what extent the transient response of Langmuir turbulence to abrupt surface heating as described in the previous sections is affected by different surface wave forcing, we compare the LT case with four additional Langmuir turbulence cases (Table I) with a weaker surface Stokes drift u_0^S (thus larger La_t, LT2 and LT3) or with a smaller decay length scale δ^S (LT4 and LT5). To assist in the comparison, we also show the results from an auxiliary run that represents the decay of convective turbulence [25]. The setup of this auxiliary run (hereafter denoted as CT) is the same as other runs, except that the initial turbulent flows before the abrupt onset of surface heating are driven by a steady surface cooling of 50 W m^{-2} without surface

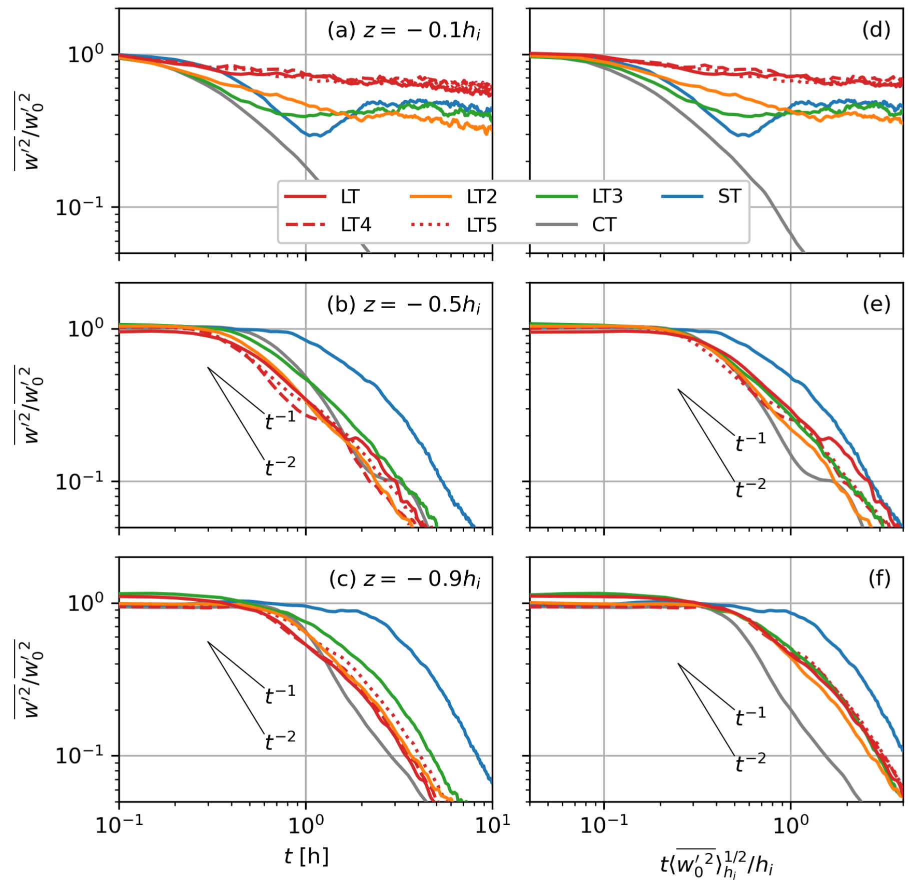

FIG. 7. Transient response of the vertical velocity variance $\overline{w'^2}$ to abrupt onset of surface heating with $Q_0 = 200$ W m^{-2} at (a,d) $z = -0.1h_i$, (b,e) $z = -0.5h_i$, and (c,f) $z = -0.9h_i$ in different cases with different surface wave forcing (colored lines). The $\overline{w'^2}$ is normalized by its mean value ($\overline{w_0'^2}$) averaged over an inertial period before the onset of surface heating (from $t = -16$ h to $t = 0$ h). The time in the right panels (d–f) are normalized by $\overline{w_0'^2}$ averaged over the initial mixed layer $\langle\overline{w_0'^2}\rangle_{h_i}$ and h_i. Slopes in (b,c,e,f) show the power relation of t^{-1} and t^{-2} as a reference.

wind and waves. The initial depth of the mixed layer at the beginning of surface heating is $h_i = 35.8$ m. For demonstration purposes, we only include the CT case with surface heating of $Q_0 = 200$ W m^{-2}. Different magnitudes of surface heating result in almost identical response (decay) of convective turbulence except very close to the surface where strong stratification develops.

Fig. 7 compare the transient response of the vertical velocity variance $\overline{w'^2}$ to the abrupt onset of surface heating with $Q_0 = 200$ W m^{-2} in different cases. Near the surface at

$z = -0.1h_i$, a weaker surface Stokes drift leads to closer resemblance of the ST case. For example, the evolution of $\overline{w'^2}$ shows two distinct phases in the LT3 case, with a rapid decay before $t \sim 1$ h followed by a weak partial recovery, but not in the LT2 case, which shows more similarity to the LT case but faster decay due to weaker Langmuir turbulence (Fig. 7a). However, the initial rapid decay in the LT3 case is faster than in the ST case, more similar to the CT case. This suggests a faster decay of the larger-scale Langmuir cells, which show some similarities with the convective plumes. On the other hand, reducing the decay length scale of the Stokes drift in the LT4 and LT5 cases does not seem to change the decay rate of $\overline{w'^2}$ too much.

Below the surface at both $z = -0.5h_i$ and $z = -0.9h_i$, the evolution of $\overline{w'^2}$ shows similar correlations with surface wave forcing. With weaker surface Stokes drift, the decay of $\overline{w'^2}$ starts later, showing more influences of wind-driven shear turbulence as in the ST case. The decay length scale of the Stokes drift changes the decay of $\overline{w'^2}$ in a subtler way. There is a noticeable delay of decay of $\overline{w'^2}$ at $z = -0.9h_i$ in the LT5 case compared to the LT case (Fig. 7c), probably due to the less coherent Langmuir cells of large scale in the LT5 case in which Stokes drift shear is restricted in a shallower region. Rescaling the time using the initial mixed layer averaged vertical velocity variance $\langle\overline{w_0'^2}\rangle_{h_i}$ and h_i reduces the spread of the transient response of Langmuir turbulence in different cases (Fig. 7d–f). This is especially true for the starting time of decay at $z = -0.5h_i$ and $z = -0.9h_i$, which is earlier than in the ST case but somewhat later than in the CT case. Unlike in the CT case, in which the decay of $\overline{w'^2}$ follows a t^{-2} power law [25], the decay of $\overline{w'^2}$ in the Langmuir turbulence cases below the surface seems to follow a t^{-1} power law initially (roughly $t < 2$ h), consistent with the results of Ref. [16], but then transits to the t^{-2} power law later. This transition to the t^{-2} power law may indicate a loss of the characteristic anisotropy of Langmuir turbulence at later times when the downwelling plumes start to resemble convective plumes in the CT case [39].

The above conclusions on the decay of Langmuir turbulence at $z = -0.9h_i$ can be extended to cases with weaker or stronger surface heating, as shown in Fig. 8. Significantly slower decay of $\overline{w'^2}$ than in the cases with $Q_0 = 200$ W m^{-2} is seen in the LT, LT4 and LT5 cases with $Q_0 = 50$ W m^{-2} (thin lines in red). In these cases, the surface heating is not strong enough to prevent the downwelling plumes of Langmuir turbulence from reaching the bottom of the mixed layer, so that the evolution of $\overline{w'^2}$ does not purely reflect the decay of

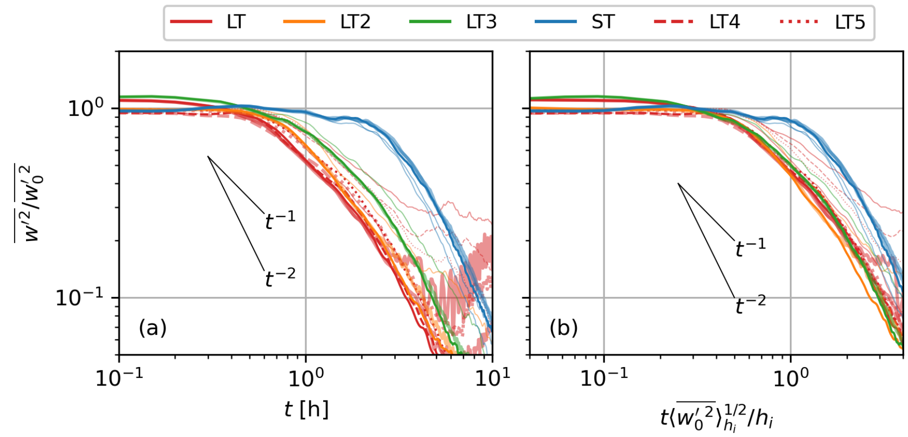

FIG. 8. Same as Fig. 7c,f, but for all cases in Table I. Thick and thin semi-transparent lines show cases with surface heating Q_0 larger and smaller than 200 W m^{-2}, respectively.

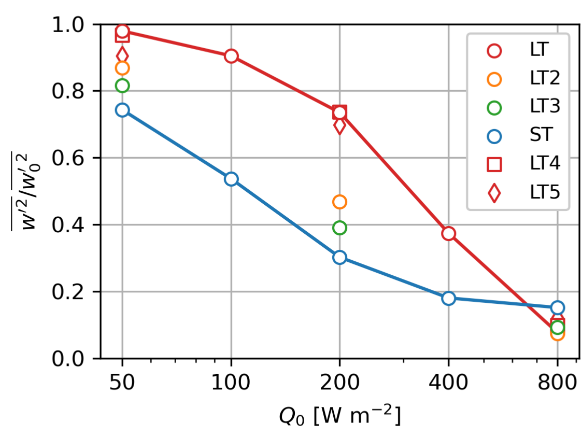

FIG. 9. The ratio of $\overline{w'^2}$ to its initial value before the onset of surface heating at $z = -0.1h_i$ and $t = 1$ h for all cases.

Langmuir turbulence. With $Q_0 = 800$ W m^{-2} (thick lines in red), intense internal waves are generated near the surface by inertially oscillating velocity shear as stratification increases, propagating downward and affecting $\overline{w'^2}$ at $z = -0.9h_i$ after around $t = 5$ h. Rescaling the time using $\langle\overline{w_0'^2}\rangle_{h_i}$ and h_i seems to collapse the curves for all other Langmuir turbulence cases (Fig. 8b). This suggests that there may exist a simple scaling law to describe the decay of Langmuir turbulence, though it should be noted that the forcing conditions explored here are rather limited.

This rescaling of time does not seem to be as helpful in collapsing the curves at $z =$

$-0.1h_i$ as at deeper depths (Fig. 7a,d), suggesting the complex competition between Stokes production of TKE and buoyancy destruction (Fig. 6a). It is beyond the scope of this study to explore a scaling law to describe the complex relationship between Stokes production of TKE and buoyancy destruction at the surface, which requires a larger set of LES that span a much wider range of forcing conditions. However, using this limited set of LES, we can still qualitatively describe the effect of surface wave forcing on the initial response of Langmuir turbulence to an abrupt onset of surface heating near the surface.

Fig. 9 shows the ratio of $\overline{w'^2}$ to its initial value before the onset of surface heating at $z = -0.1h_i$ and $t = 1$ h for all cases. This is a measure of the initial decay of $\overline{w'^2}$ near the surface, which is not necessarily exponential, but certainly monotonic, for all cases (not shown). Except for the cases with $Q_0 = 800$ W m^{-2}, $\overline{w'^2}$ decays the fastest in the ST case and the slowest in the LT case, with progressively stronger surface wave forcing (lower value of La_t) leading to progressively slower decay as shown by the LT2 and LT3 cases. The e-folding depth of Stokes drift δ^S also affects the initial decay of $\overline{w'^2}$, with shallower δ^S corresponding to faster decay, as shown by the LT4 and LT5 cases. This is probably because the driving force of Langmuir turbulence (Stokes drift shear) is more confined near the surface for shallower δ^S, and thus is more affected by surface heating. For the cases with $Q_0 = 800$ W m^{-2}, $\overline{w'^2}$ decreases to less than 20% of its initial value at $t = 1$ h and shows less dependence on surface wave forcing. Interestingly, the decay of $\overline{w'^2}$ seems to level off beyond $Q_0 = 400$ W m^{-2} in the ST case, but not in the LT case, likely due to the breakdown of Langmuir cells in the latter which further decreases $\overline{w'^2}$.

IV. DISCUSSION AND CONCLUSIONS

In this study, we investigated the transient response of Langmuir turbulence to an abrupt onset of surface heating using a set of idealized LES. This complements previous studies on the equilibrium response of Langmuir turbulence under steady surface heating by, e.g., Refs. [7, 16, 41]. We compared the results with the transient response of wind-driven shear turbulence under the same surface heating conditions. Near the surface, enhanced vertical mixing by Langmuir turbulence inhibits the formation of near-surface stratification, and the intensity of Langmuir turbulence decreases monotonically after the onset of surface heating. This is in contrast to wind-driven shear turbulence, which is initially suppressed by the formation of strong near-surface stratification but later partially recovers due to the development of strong shear in the near-surface warm layer. Under sufficiently strong surface heating, Langmuir cells break down and the results become similar to the wind-driven shear turbulence. These results are consistent with the existing literature on the dynamics of DWL [19–23], the effect of Langmuir turbulence on DWL [18, 24], and the breakdown of Langmuir turbulence under strong surface heating [41].

Below the surface, sufficiently strong surface heating effectively blocked the connection between the deeply penetrating downwelling plumes due to Langmuir turbulence and their driving force near the surface, where Stokes drift shear is strong, resulting in almost immediate decay of these large-scale coherent structures. This is similar to the decay of convective turbulence, in which convective cells quickly decay after losing their driving force with the onset of surface heating [25], and occurs much earlier (after a short steady period of ∼15–30 minutes depending on the depth) than the decay of wind-driven shear turbulence (which occurs after a steady period of ∼1–2 hours). With the help of coherent downwelling plumes in Langmuir turbulence, the effect of changes in surface heating is felt much quicker at depth than the wind-driven shear turbulence. But different from the decay of convective turbulence, in which the vertical velocity variance decays at a rate following t^{-2} [25], the vertical velocity variance of Langmuir turbulence decays at a rate initially following t^{-1} [16] and later transitioning to t^{-2}. This transition of the decay rate seems to be robust in different cases with different surface forcing. An investigation of its mechanisms and timing is left for future research.

We also explored the impact of surface wave forcing on the transient response of Langmuir turbulence by varying the surface value of Stokes drift (thus La_t) or its decay depth δ^S. With progressively weaker surface wave forcing (larger La_t), the transient response of Langmuir turbulence progressively approaches that of wind-driven shear turbulence. Shallower decay depth of Stokes drift appears to result in a slightly earlier decrease of $\overline{w'^2}$ near the surface, but a slightly later decay at depth, probably due to less coherent downwelling plumes in these cases. Rescaling the time using the initial mixed layer averaged vertical velocity variance $\langle\overline{w_0'^2}\rangle_{h_i}$ and the initial mixed layer depth h_i seems to collapse the curves for the decay of $\overline{w'^2}$ at depth. Thus, existing scaling laws of $\langle\overline{w_0'^2}\rangle_{h_i}$ for Langmuir turbulence such as Refs. [26, 44] could potentially be useful. However, the significantly quicker response of $\overline{w'^2}$ to changes of surface forcing in Langmuir turbulence than in wind-driven shear turbulence calls for further investigation of the possible dependence on factors other than $\langle\overline{w_0'^2}\rangle_{h_i}$ and h_i. The response of $\overline{w'^2}$ near the surface is more complex due to the competition between destabilizing Stokes shear force and stabilizing surface heating. It is beyond the scope of this study to explore a scaling law that describes the near-surface behavior of Langmuir turbulence to the abrupt onset of surface heating. A larger set of LES that covers a wider range of forcing conditions is likely needed. In addition, penetrative solar radiation will surely affect the response of Langmuir turbulence differently than surface heating [e.g., 16]. Since the penetration depth of solar radiation is often of magnitude similar to the decay depth of Stokes drift, quantifying the competition between the destabilizing Stokes shear force and stabilizing solar radiation is even more challenging. Similar LES simulations with an abrupt onset of penetrative solar radiation are currently underway to explore its effects.

Nevertheless, these results have important implications for parameterizing vertical mixing due to Langmuir turbulence under transient forcing conditions, such as in the early morning during a diurnal cycle as introduced in Section I. Existing Langmuir turbulence parameterizations based on the popular K-Profile Parameterizations [45] such as Ref. [13] (see also a recent review in Ref. [15]) produce instantaneous response of turbulent fluxes to the changes of surface forcing, assuming that the turbulence adjusts quickly into an equilibrium state. As shown here, this assumption fails when the surface forcing changes sufficiently fast. The transient response of Langmuir turbulence can occur over a time period of a few hours or longer. Modifications will be needed in these parameterizations to account for the transient response of the turbulence statistics to the varying surface forcing. One possible route forward may be to relax the equilibrium assumption by incorporating a transient response time scale that depends on the forcing conditions. In addition, even Langmuir turbulence parameterizations based on two-equation models such as Ref. [11], which evolve prognostic equations of the TKE and a turbulent length scale (thus having memories of previous turbulence state), may require modifications to account for the differential decay rates of the three components of the TKE (thus the anisotropy of turbulence) in Langmuir turbulence, perhaps by modifying the closure model for the pressure-strain terms (see, e.g., Ref. [46]). Exploration of these ideas in a Langmuir turbulence parameterization is left for future research.

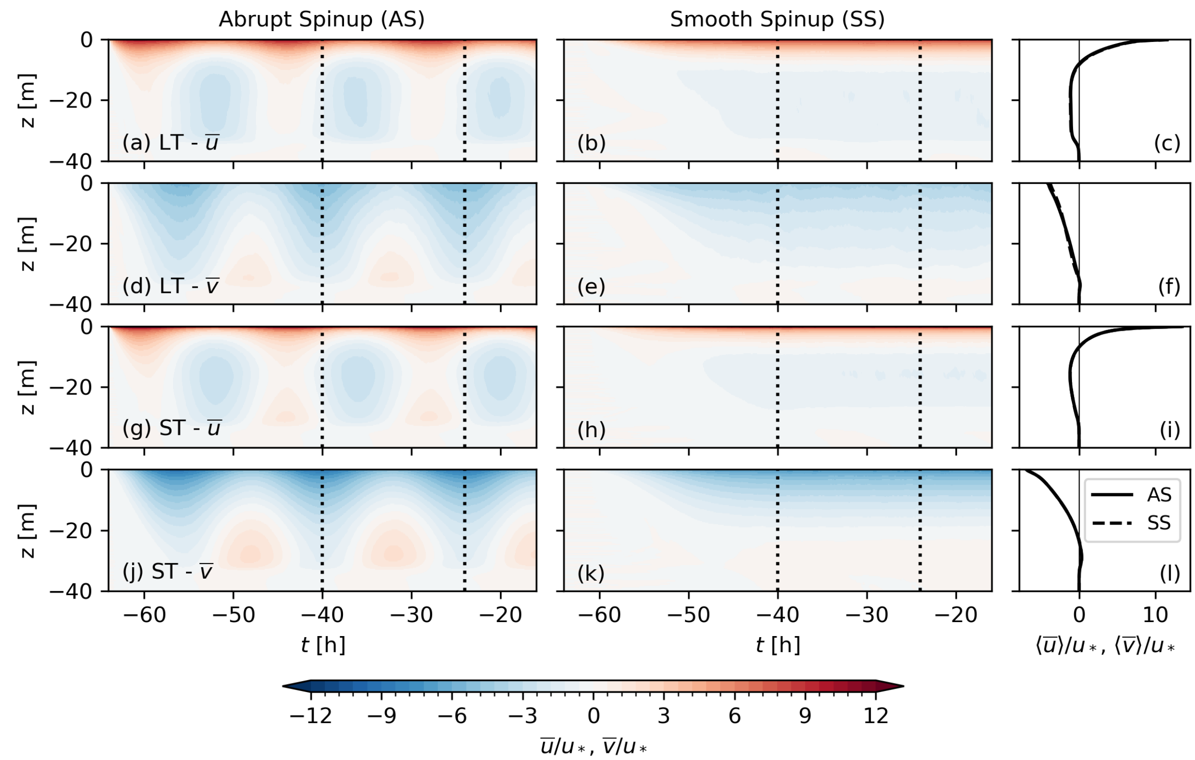

FIG. 10. Comparison between (a,d,g,j) an abrupt spinup (AS) with a sudden onset of the surface wind at the beginning of the simulation and (b,e,h,k) a smooth spinup (SS) with surface wind stress gradually increasing to the target value using a time-dependent scaling factor according to (5). The left two columns show the time evolution of horizontally averaged velocity $\overline{u}$ and $\overline{v}$ in the LT and ST cases. Solid and dashed lines in the right column show the mean profiles of velocity $\langle\overline{u}\rangle$ and $\langle\overline{v}\rangle$ for the abrupt and smooth spinup, respectively, averaged over the first inertial period after the smooth onset of surface wind stress (between dotted lines in the left two columns). The velocity components are normalized by the friction velocity u_*.

Appendix A: Abrupt Versus Smooth Spinup

The effect of a "Smooth Spinup" with gradually increasing surface wind stress by applying the scaling factor in Equation (5) is demonstrated in Fig. 10 by comparing to an "Abrupt Spinup" in which steady surface wind stress is applied at the beginning of the simulation at $t = -64$ h. While significant inertial oscillations of $\overline{u}$ and $\overline{v}$ are seen in both ST and LT cases with "Abrupt Spinup", they are almost completely suppressed with "Smooth Spinup". As shown in the right column, the mean profiles for $\overline{u}$ and $\overline{v}$ averaged over an inertial period

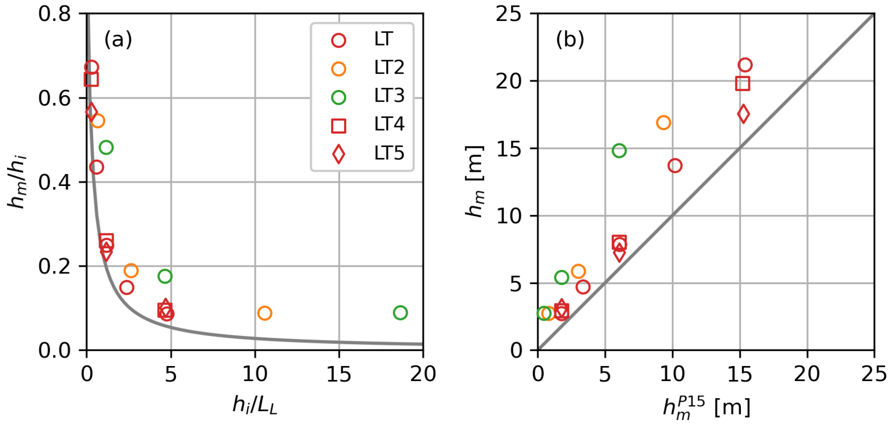

FIG. 11. Comparison between the equilibrium mixed layer depth h_m in our Langmuir turbulence simulations with the scaling in [16]. In panel (a), h_m/h_i is plotted against h_i/L_L (where $L_L = -u_*^2 u_0^S/B_0$), corresponding to Fig. 10a in [16], in which the gray curve shows the scaling according to their Equation (4). In panel (b), h_m is plotted directly against the value derived from the scaling in [16] h_m^{P15}.

are not changed by the different spinup strategies.

Appendix B: Equilibrium Mixed Layer Depth

The equilibrium mixed layer depth under the combined forcing of Langmuir turbulence and surface heating in our simulations is compared with the scaling according to Equation (4) in Ref. [16] in Fig. 11. As shown in panel (a), the equilibrium mixed layer depth in our simulations is generally consistent with the scaling in Ref. [16], but seems to be systematically deeper, which is better illustrated in panel (b). This is probably due to the much stronger surface heating (thus, smaller $L_L = -u_*^2 u_0^S/B_0$) used in our simulations than in Ref. [16]. In particular, the range of h_i/L_L covered in the set of LES here (up to 18) is much larger than that of Ref. [16] (less than 3). So, it is likely that the turbulence in our simulations with stronger surface heating may not have reached an equilibrium state after 48 hours of surface heating, which may explain the deeper h_m seen here. Given our focus on the transient response of Langmuir turbulence in the initial stage after the onset of surface heating, it may not be necessary to run these simulations into equilibrium, which may require much longer simulations.

ACKNOWLEDGMENTS

We sincerely thank two anonymous reviewers for their very helpful comments and suggestions. This work is supported by the National Natural Science Foundation of China (42206031), a grant from the Research Grants Council of the Hong Kong Special Administrative Region, China (AoE/P-601/23-N), and the Guangdong Provincial Project (2023QN10H423).

DATA AVAILABILITY STATEMENTS

The data that support the findings of this article are openly available [47].

---

[1] L. Cavaleri, B. Fox-Kemper, and M. Hemer, Wind waves in the coupled climate system, Bulletin of the American Meteorological Society **93**, 1651 (2012).

[2] S. E. Belcher, A. L. M. Grant, K. E. Hanley, B. Fox-Kemper, L. Van Roekel, P. P. Sullivan, W. G. Large, A. Brown, A. Hines, D. Calvert, A. Rutgersson, H. Pettersson, J.-R. Bidlot, P. A. E. M. Janssen, and J. A. Polton, A global perspective on Langmuir turbulence in the ocean surface boundary layer, Geophysical Research Letters **39**, L18605 (2012).

[3] A. D. D. Craik and S. Leibovich, A rational model for Langmuir circulations, Journal of Fluid Mechanics **73**, 401 (1976).

[4] S. Leibovich, The form and dynamics of Langmuir circulations, Annual Review of Fluid Mechanics **15**, 391 (1983).

[5] S. A. Thorpe, Langmuir circulation, Annual Review of Fluid Mechanics **36**, 55 (2004).

[6] J. C. McWilliams, P. P. Sullivan, and C.-H. Moeng, Langmuir turbulence in the ocean, Journal of Fluid Mechanics **334**, 1 (1997).

[7] M. Li, C. Garrett, and E. D. Skyllingstad, A regime diagram for classifying turbulent large eddies in the upper ocean, Deep-Sea Research Part I: Oceanographic Research Papers **52**, 259 (2005).

[8] E. A. D'Asaro, Turbulence in the upper-ocean mixed layer., Annual Review of Marine Science **6**, 101 (2014).

[9] Q. Li, A. Webb, B. Fox-Kemper, A. Craig, G. Danabasoglu, W. G. Large, and M. Vertenstein, Langmuir mixing effects on global climate: WAVEWATCH III in CESM, Ocean Modelling **103**, 145 (2016).

[10] L. H. Kantha and C. A. Clayson, On the effect of surface gravity waves on mixing in the oceanic mixed layer, Ocean Modelling **6**, 101 (2004).

[11] R. R. Harcourt, An improved second-moment closure model of Langmuir turbulence, Journal of Physical Oceanography **45**, 84 (2015).

[12] B. G. Reichl, D. Wang, T. Hara, I. Ginis, and T. Kukulka, Langmuir turbulence parameterization in tropical cyclone conditions, Journal of Physical Oceanography **46**, 863 (2016).

[13] Q. Li and B. Fox-Kemper, Assessing the effects of Langmuir turbulence on the entrainment buoyancy flux in the ocean surface boundary layer, Journal of Physical Oceanography **47**, 2863 (2017).

[14] B. G. Reichl and Q. Li, A parameterization with a constrained potential energy conversion rate of vertical mixing due to Langmuir turbulence, Journal of Physical Oceanography **49**, 2935 (2019).

[15] Q. Li, B. G. Reichl, B. Fox-Kemper, A. Adcroft, S. Belcher, G. Danabasoglu, A. Grant, S. M. Griffies, R. W. Hallberg, T. Hara, R. Harcourt, T. Kukulka, W. G. Large, J. C. McWilliams, B. Pearson, P. Sullivan, L. Van Roekel, P. Wang, and Z. Zheng, Comparing ocean surface boundary vertical mixing schemes including Langmuir turbulence, Journal of Advances in Modeling Earth Systems **11**, 3545 (2019).

[16] B. C. Pearson, A. L. M. Grant, J. A. Polton, and S. E. Belcher, Langmuir turbulence and surface heating in the ocean surface boundary layer, Journal of Physical Oceanography **45**, 2897 (2015).

[17] W. G. Large, E. G. Patton, and P. P. Sullivan, The diurnal cycle of entrainment and detrainment in LES of the southern ocean driven by observed surface fluxes and waves, Journal of Physical Oceanography **51**, 3253 (2021).

[18] X. Wang, T. Kukulka, J. T. Farrar, A. J. Plueddemann, and S. F. Zippel, Langmuir turbulence controls on observed diurnal warm layer depths, Geophysical Research Letters **50**, e2023GL103231 (2023).

[19] J. F. Price, R. A. Weller, and R. Pinkel, Diurnal cycling: Observations and models of the upper ocean response to diurnal heating, cooling, and wind mixing, Journal of Geophysical

Research **91**, 8411 (1986).

[20] C. W. Fairall, E. F. Bradley, J. S. Godfrey, G. A. Wick, J. B. Edson, and G. S. Young, Cool-skin and warm-layer effects on sea surface temperature, Journal of Geophysical Research: Oceans **101**, 1295 (1996).

[21] G. Sutherland, L. Marié, G. Reverdin, K. H. Christensen, G. Broström, and B. Ward, Enhanced turbulence associated with the diurnal jet in the ocean surface boundary layer, Journal of Physical Oceanography **46**, 3051 (2016).

[22] K. G. Hughes, J. N. Moum, and E. L. Shroyer, Evolution of the velocity structure in the diurnal warm layer, Journal of Physical Oceanography **50**, 615 (2020).

[23] K. G. Hughes, J. N. Moum, E. L. Shroyer, and W. D. Smyth, Stratified shear instabilities in diurnal warm layers, Journal of Physical Oceanography **51**, 2583 (2021).

[24] T. Kukulka, A. J. Plueddemann, and P. P. Sullivan, Inhibited upper ocean restratification in nonequilibrium swell conditions, Geophysical Research Letters **40**, 3672 (2013).

[25] F. T. M. Nieuwstadt and R. A. Brost, The decay of convective turbulence, Journal of the Atmospheric Sciences **43**, 532 (1986).

[26] R. R. Harcourt and E. A. D'Asaro, Large-eddy simulation of Langmuir turbulence in pure wind seas, Journal of Physical Oceanography **38**, 1542 (2008).

[27] C. A. Paulson and J. J. Simpson, Irradiance measurements in the upper ocean, Journal of Physical Oceanography **7**, 952 (1977).

[28] A. Ramadhan, G. Wagner, C. Hill, J.-M. Campin, V. Churavy, T. Besard, A. Souza, A. Edelman, R. Ferrari, and J. Marshall, Oceananigans.jl: Fast and friendly geophysical fluid dynamics on GPUs, Journal of Open Source Software **5**, 2018 (2020).

[29] G. L. Wagner, G. P. Chini, A. Ramadhan, B. Gallet, and R. Ferrari, Near-inertial waves and turbulence driven by the growth of swell, Journal of Physical Oceanography **51**, 1337 (2021).

[30] G. L. Wagner, N. Pizzo, L. Lenain, and F. Veron, Transition to turbulence in wind-drift layers, Journal of Fluid Mechanics **976**, A8 (2023).

[31] X. Fan, B. Fox-Kemper, N. Suzuki, Q. Li, P. Marchesiello, P. P. Sullivan, and P. S. Hall, Comparison of the Coastal and Regional Ocean COmmunity model (CROCO) and NCAR-LES in non-hydrostatic simulations, Geoscientific Model Development **17**, 4095 (2024).

[32] J. Huang, M. Chamecki, Q. Li, and B. Chen, The role of longitudinal alignment between surface and bottom forcing on the full-column turbulence mixing in the coastal ocean, Ocean

Modelling **199**, 102637 (2026).
[33] Z. Wei, Q. Li, and B. Chen, A direct assessment of Langmuir turbulence parameterizations in idealized coastal merging boundary layers, Journal of Advances in Modeling Earth Systems **18**, e2025MS004993 (2026).
[34] Q. Li, Large eddy simulations of stabilizing effects induced by opposing Eulerian current and Stokes drift in an idealized ocean surface boundary layer, Journal of Physical Oceanography (2026), under review.
[35] D. D. Holm, The ideal Craik-Leibovich equations, Physica D: Nonlinear Phenomena **98**, 415 (1996).
[36] N. Suzuki and B. Fox-Kemper, Understanding Stokes forces in the wave-averaged equations, Journal of Geophysical Research: Oceans **121**, 3579 (2016).
[37] R. Verstappen, How much eddy dissipation is needed to counterbalance the nonlinear production of small, unresolved scales in a large-eddy simulation of turbulence?, Computers & Fluids **176**, 276 (2018).
[38] K. G. Pressel, S. Mishra, T. Schneider, C. M. Kaul, and Z. Tan, Numerics and subgrid-scale modeling in large eddy simulations of stratocumulus clouds, Journal of Advances in Modeling Earth Systems **9**, 1342 (2017).
[39] Q. Li and B. Fox-Kemper, Anisotropy of Langmuir turbulence and the Langmuir-enhanced mixed layer entrainment, Physical Review Fluids **5**, 013803 (2020).
[40] J. A. Polton and S. E. Belcher, Langmuir turbulence and deeply penetrating jets in an unstratified mixed layer, Journal of Geophysical Research: Oceans **112**, 1 (2007).
[41] H. S. Min and Y. Noh, Influence of the surface heating on Langmuir circulation, Journal of Physical Oceanography **34**, 2630 (2004).
[42] A. L. M. Grant and S. E. Belcher, Characteristics of Langmuir turbulence in the ocean mixed layer, Journal of Physical Oceanography **39**, 1871 (2009).
[43] T. Kukulka and R. R. Harcourt, Influence of Stokes drift decay scale on Langmuir turbulence, Journal of Physical Oceanography **47**, 1637 (2017).
[44] L. Van Roekel, B. Fox-Kemper, P. P. Sullivan, P. E. Hamlington, and S. R. Haney, The form and orientation of Langmuir cells for misaligned winds and waves, Journal of Geophysical Research **117**, C05001 (2012).

[45] W. G. Large, J. C. Mcwilliams, and S. C. Doney, Oceanic vertical mixing: A review and a model with a nonlocal boundary layer parameterization, Reviews of Geophysics **32**, 363 (1994).

[46] B. C. Pearson, A. L. M. Grant, and J. A. Polton, Pressure–strain terms in Langmuir turbulence, Journal of Fluid Mechanics **880**, 5 (2019).

[47] W. Pan and Q. Li, Code and notebooks that support the paper "Transient response of Langmuir turbulence to abrupt onset of surface heating" (2026).